A General Single-Sensor Damping Framework for LCL-Equipped High-Speed PMSM Drives

Yao, Yu; Huang, Yunkai; Peng, Fei; Dong, Jianning; Zhu, Zichong

DOI
10.1109/TIE.2022.3186342

Publication date
2022

Document Version
Final published version

Published in
IEEE Transactions on Industrial Electronics

Letters

A General Single-Sensor Damping Framework for *LCL*-Equipped High-Speed PMSM Drives

Yu Yao, Yunkai Huang, Fei Peng, Jianning Dong, and Zichong Zhu

***Abstract*—This letter proposes a general single-sensor active damping framework for *LCL*-equipped high-speed permanent magnet synchronous machines. By the proposed method, arbitrary damping assignment and stability for the *LCL* resonance within the Nyquist frequency are achieved with only the inverter-current feedback or motor-current feedback. Moreover, the simplified analytical expression between the physical parameters and the damping performance enables automatic tuning for different drive systems.**

***Index Terms*—General single-sensor resonance damping, HSPMSM, *LCL* filter, wide stable region.**

I. Introduction

HIGH-SPEED surface-mounted permanent magnet synchronous machines (HSPMSMs) are widely used in industrial applications because of their high power density and high efficiency [1]. For HSPMSM drives, an *LC* or *LCL* output filter is often added to eliminate the excessive dv/dt voltage, additional losses in the motor resulting from current harmonics, and high-frequency electromagnetic noise in the motor cable. However, the *LCL* circuit introduces a resonance peak and it may damage the stability of the current control loop.

Some active damping (AD) strategies are developed effectively to deal with this *LCL* resonance problem. Based on the damping principle, they can be classified into the following categories: filter-based methods, partial-state feedback (PSF) method, full-state feedback control (FSFC) methods, observer-based FSFC (OFSFC), and equivalent FSFC (EFSFC) methods.

Manuscript received 4 January 2022; revised 6 May 2022; accepted 11 June 2022. Date of publication 1 July 2022; date of current version 3 January 2023. This work was supported by National Natural Science Foundation of China under Grant 51777034 and Grant 51707037 and by the Excellence Project Funds of Southeast University. *(Corresponding author: Yu Yao.)*

Yu Yao, Yunkai Huang, and Fei Peng are with the School of Electrical Engineering, Southeast University, Nanjing 210096, China (e-mail: yuyao@seu.edu.cn; huangyk@seu.edu.cn; pengfei@seu.edu.cn).

Jianning Dong is with the Delft University of Technology, 2628, CD Delft, The Netherlands (e-mail: j.dong-4@tudelft.nl).

Zichong Zhu is with the School of Electrical Engineering and Control Science, Nanjing Tech University, Nanjing 211816, China (e-mail: zhu_zichong@njtech.edu.cn).

Color versions of one or more figures in this article are available at https://doi.org/10.1109/TIE.2022.3186342.

Digital Object Identifier 10.1109/TIE.2022.3186342

In filter-based methods, the notch filter [2] is commonly used to provide the additional phase lead or phase lag. In PSF methods, the AD effect is induced by the partial state feedback, including the proportional capacitor current feedback [3], the filtered capacitor current feedback [4], the filtered capacitor voltage feedback [5], the high-pass grid-current feedback [6], and the inverter-current feedback [7]. Among filter-based methods and PSF methods, the resonance damping ratio cannot be freely designed and the stability is usually restricted by the location of the *LCL* resonance due to the digital computation delay. To achieve a strong resonance damping, FSFC methods are developed with arbitrary pole placement [8], and, thus the damping ratio is freely selected by users at any resonance frequency, but it requires the measurement of all the states. To reduce the number of sensors, the OFSFC methods [9]–[11] are designed by introducing a high-order model-based state observer (three orders in the stationary coordinate while six orders in the synchronous coordinate). Clearly, it sharply increases the computational complication and relies on the accuracy of the system parameters. To eliminate the state-observer, in [12], the equivalent feedback is proposed based on the filtering of the control action and in that way, the single-sensor EFSFCC is achieved with arbitrary pole assignment, but it requires the calculation of the state-feedback gain matrix for an extended high-order drive system (at least 6). Furthermore, the analytical expression of the feedback-gain matrix between the physical system parameters and the damping effect is very complicated, and thus it brings many difficulties for microcontrollers to automatically calculate the gain matrix with respect to different drive systems.

To address these issues, this letter proposes a general single-sensor AD framework for *LCL*-equipped HSPMSMs in the synchronous coordinate, which has the following advantages as:

1) effective for the inverter-current feedback (ICF) and motor-current feedback (MCF) drive system;
2) single-sensor synchronous AD strategy for motor drives;
3) simplified analytical expression between the physical parameters and the damping performance, which enables automatic tuning for different drive systems;
4) arbitrary damping assignment and stability for the *LCL* resonance within the Nyquist frequency.

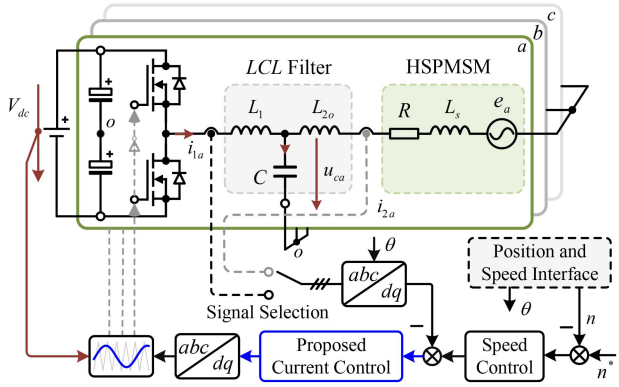

Fig. 1. General control structure of single-sensor HSPMSMs drive system equipped with *LCL* filter.

II. General Discrete-Time Model

Fig. 1 shows the general control structure of the *LCL*-equipped HSPMSM drives. Without loss of generality, the measured state can be the inverter current or the motor current. According to [3], [13], the discrete-time transfer function of the inverter current can be obtained as

$$G_{i_1}(z) = \frac{i_{1s}(z)}{V_s(z)} = \frac{T}{(L_1+L_2)(z-1)} + \frac{L_2}{L_1+L_2}\frac{\sin(\omega_{res}T)}{\omega_{res}L_1}\frac{z-1}{z^2-2z\cos(\omega_{res}T)+1} \tag{1}$$

and

$$G_{i_2}(z) = \frac{i_{2s}(z)}{V_s(z)} = \frac{T}{(L_1+L_2)(z-1)} - \frac{\sin(\omega_{res}T)}{\omega_{res}(L_1+L_2)}\frac{z-1}{z^2-2z\cos(\omega_{res}T)+1} \tag{2}$$

where $\omega_{res} = 2\pi f_{res} = \sqrt{(L_1+L_2)/(L_1L_2C)}$ is the natural resonant frequency, L_1 is the inverter-side inductance, $L_2 = L_{2o} + L_s$, L_{2o} is the motor-side inductance, L_s is the motor inductance, C refers to the filtered capacitor, $i_{1s} = i_{1\alpha} + ji_{1\beta}$ is the inverter current, and $i_{2s} = i_{2\alpha} + ji_{2\beta}$ denotes the motor current. $V_s = V_\alpha + jV_\beta$ denotes the output voltage. T is the sampling period.

To represent the transfer function in the synchronous coordinate, the general discrete-time model of *LCL*-equipped HSPMSM drives as

$$G_r(z) = \frac{i_r(z)}{V_r(z)} = \frac{1}{z}\frac{g_1z^2e^{2j\omega_eT} + g_2ze^{j\omega_eT} + g_1}{z^3e^{3j\omega_eT} - g_3z^2e^{2j\omega_eT} + g_3ze^{j\omega_eT} - 1} \tag{3}$$

where $i_r = i_{1,2d} + ji_{1,2q}$ is the inverter-current or motor-current complex vector. $V_r = V_d + jV_q$. $\omega_e = 2\pi f_e$ is the fundamental angular frequency. Besides, g_1, g_2, g_3, and μ_1 are defined as

$$g_1 = (\mu_1+\mu_2) \quad g_2 = -2(\mu_2 + \mu_1\cos(\omega_{res}T)) \quad g_3 = (2\cos(\omega_{res}T)+1) \quad \mu_1 = T/(L_1+L_2). \tag{4}$$

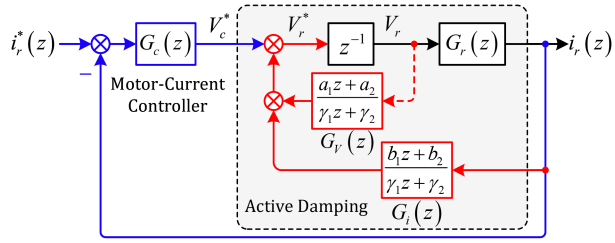

Fig. 2. Structure of the proposed general single-sensor AD method.

For the ICF system, μ_2 is defined as

$$\mu_2 = \frac{L_2}{L_1+L_2}\frac{\sin(\omega_{res}T)}{\omega_{res}L_1} \tag{5}$$

and for the MCF system, μ_2 is defined as

$$\mu_2 = -\frac{1}{L_1+L_2}\frac{\sin(\omega_{res}T)}{\omega_{res}}. \tag{6}$$

Considering the digital delay, the synchronous discrete-time model of *LCL*-equipped HSPMSM is derived as [14]

$$G_p(z) = \frac{i_r(z)}{V_r^*(z)} = z^{-1}G_r(z) \tag{7}$$

where V_r^* represents the complex voltage reference.

III. Proposed General Single-Sensor AD Method

Fig. 2 demonstrates the overall structure of the proposed general single-sensor AD method. The proposed current control law consists of the current controller and the AD part, which can be expressed as

$$V_r^*(z) = \underbrace{G_c(z)(i_r^* - i_r)}_{current\ \ controller} + \underbrace{G_V(z)V_r(z) + G_i(z)i_r(z)}_{AD} \tag{8}$$

where i_r^* is the current reference. $G_c(z)$, $G_V(z)$, and $G_i(z)$ denote the current controller, the output voltage AD controller, and the current AD controller, respectively. More details of the motor-current controller can be found in [14], which is given in (9). This letter will focus on the design and analysis of the AD control method

$$G_c(z) = \frac{V_c^*(z)}{i_r^*(z) - i_r(z)} = \frac{ze^{j\omega_eT} - e^{-\frac{R}{L_2}T}}{z-1}\frac{az+b}{z-1} \tag{9}$$

where a and b are control coefficients.

A. AD Controller Design

The output voltage AD controller and the current AD controller are designed as

$$G_V(z) = \frac{a_1z+a_2}{\gamma_1z+\gamma_2} \quad G_i(z) = \frac{b_1z+b_2}{\gamma_1z+\gamma_2} \tag{10}$$

where γ_1, γ_2, a_1, a_2, b_1, and b_2 are AD coefficients. γ_1 and γ_2 are real values while the rest are complex values.

Based on Fig. 2, the transfer function from the output of $G_c(z)$ to the measured current i_r can be calculated as

$$G_{damp}(z) = \frac{i_r(z)}{V_c^*(z)} = \frac{P(z)}{Q(z)} = \frac{z^{-1}G_r(z)}{1 - z^{-1}G_V(z) - z^{-1}G_r(z)G_i(z)} \tag{11}$$

where $G_{damp}(z)$ denotes the internal damped transfer function.

Substituting (3) and (10) into (11), it leads to

$$G_{damp}(z) = \frac{P(z)}{Q(z)} = \frac{(\gamma_1 z + \gamma_2) N(z)}{(z(\gamma_1 z + \gamma_2) - (a_1 z + a_2)) D(z) - (b_1 z + b_2) N(z)} \tag{12}$$

where $N(z)$ and $D(z)$ are defined as

$$\begin{aligned} N(z) &= g_1 z^2 e^{2j\omega_e T} + g_2 z e^{j\omega_e T} + g_1 \\ D(z) &= z^3 e^{3j\omega_e T} - g_3 z^2 e^{2j\omega_e T} + g_3 z e^{j\omega_e T} - 1. \end{aligned} \tag{13}$$

Expanding $Q(z)$, it can be derived as

$$Q(z) = \alpha_5 z^5 + \alpha_4 z^4 + \alpha_3 z^3 + \alpha_2 z^2 + \alpha_1 z + \alpha_0 \tag{14}$$

where α_i $(i = 0, 1, 2, 3, 4, 5)$ is defined as

$$\begin{aligned} \alpha_5 &= \gamma_1 e^{3j\omega_e T} \\ \alpha_4 &= (\gamma_2 - a_1) e^{3j\omega_e T} - \gamma_1 g_3 e^{2j\omega_e T} \\ \alpha_3 &= \gamma_1 g_3 e^{j\omega_e T} - (\gamma_2 - a_1) g_3 e^{2j\omega_e T} \\ &\quad - a_2 e^{3j\omega_e T} - b_1 g_1 e^{2j\omega_e T} \\ \alpha_2 &= (\gamma_2 - a_1) g_3 e^{j\omega_e T} - \gamma_1 + a_2 g_3 e^{2j\omega_e T} \\ &\quad - b_1 g_2 e^{j\omega_e T} - b_2 g_1 e^{2j\omega_e T} \\ \alpha_1 &= a_1 - \gamma_2 - a_2 g_3 e^{j\omega_e T} - b_1 g_1 - b_2 g_2 e^{j\omega_e T} \\ \alpha_0 &= a_2 - b_2 g_1. \end{aligned} \tag{15}$$

To achieve AD, $Q(z)$ should be well modified to eliminate the resonant poles. Therefore, the desired $Q(z)$ is introduced as

$$\overline{Q}(z) = (\gamma_1 z + \gamma_2) z(z e^{j\omega_e T} - 1) \times \left(z^2 e^{2j\omega_e T} - 2z e^{j\omega_e T} \cos(\overline{\omega}_{res} T) + \delta\right) \tag{16}$$

where $\overline{\omega}_{res} = 2\pi \overline{f}_{res}$ denotes the desired resonance angular frequency. δ is positive damping constant. Clearly, when $\delta < 1$, the eigenvalues of $\overline{Q}(z)$ are located within the unit circle. Expanding (16), it can be derived as

$$\overline{Q}(z) = \beta_5 z^5 + \beta_4 z^4 + \beta_3 z^3 + \beta_2 z^2 + \beta_1 z + \beta_0 \tag{17}$$

where these coefficients β_i $(i = 0, 1, 2, 3, 4, 5)$ are defined as

$$\begin{aligned} \beta_5 &= \gamma_1 e^{3j\omega_e T} \\ \beta_4 &= \left(\gamma_2 e^{j\omega_e T} - \gamma_1 - 2\gamma_1 \cos(\overline{\omega}_{res} T)\right) e^{2j\omega_e T} \\ \beta_3 &= \gamma_1 \delta e^{j\omega_e T} - 2\left(\gamma_2 e^{j\omega_e T} - \gamma_1\right) e^{j\omega_e T} \cos(\overline{\omega}_{res} T) \\ &\quad - \gamma_2 e^{2j\omega_e T} \\ \beta_2 &= \left(\gamma_2 e^{j\omega_e T} - \gamma_1\right) \delta + 2\gamma_2 e^{j\omega_e T} \cos(\overline{\omega}_{res} T) \\ \beta_1 &= -\gamma_2 \delta \\ \beta_0 &= 0. \end{aligned} \tag{18}$$

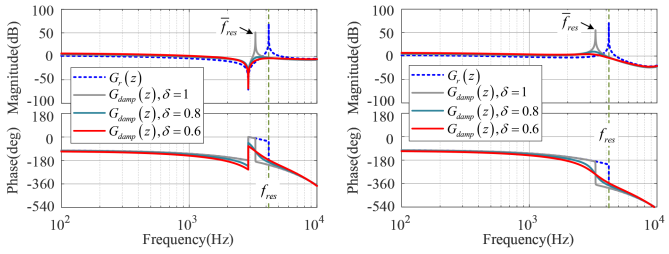

Fig. 3. Bode diagram of the damped model $G_{damp}(z)$ with f_e = 1000 Hz, $\overline{f}_{res}$ = 4500 Hz, f_{res} = 5400 Hz, and $\delta = 0.8$.

To make $Q(z) = \overline{Q}(z)$, $\alpha_i = \beta_i$ $(i = 0, 1, 2, 3, 4, 5)$ should be satisfied and it leads to

$$\begin{aligned} a_1 &= 2\gamma_1 (\cos(\overline{\omega}_{res} T) - \cos(\omega_{res} T)) e^{-j\omega_e T} \\ a_2 &= b_2 g_1 \\ b_1 &= \left(a_1 - \gamma_2 (1 - \delta) - b_2 (g_1 g_3 + g_2) e^{j\omega_e T}\right)/g_1 \\ \gamma_2 &= \frac{\Theta_{22} M_1 - \Theta_{12} M_2}{\Theta_{11}\Theta_{22} - \Theta_{12}\Theta_{21}} \quad b_2 = \frac{-\Theta_{21} M_1 + \Theta_{11} M_2}{\Theta_{11}\Theta_{22} - \Theta_{12}\Theta_{21}} \end{aligned} \tag{19}$$

where σ_3 and σ_4 are defined as

$$\begin{aligned} \Theta_{11} &= 2\cos(\overline{\omega}_{res} T) - 2\cos(\omega_{res} T) + 1 - \delta \\ \Theta_{12} &= -(g_1 - g_1 g_3 - g_2) e^{j\omega_e T} \\ \Theta_{21} &= 2\cos(\omega_{res} T) - 2\cos(\overline{\omega}_{res} T) + 1 - \delta \\ &\quad + g_2 (1 - \delta)/g_1 \\ \Theta_{22} &= 2(g_1 \cos(\omega_{res} T) + g_2 (g_1 g_3 + g_2)/g_1) e^{j\omega_e T} \\ M_1 &= 2\gamma_1 (\cos(\overline{\omega}_{res} T) - \cos(\omega_{res} T)) e^{-j\omega_e T} \\ &\quad + a_1 - a_1 g_3 + (\delta - 1) e^{-j\omega_e T} \\ M_2 &= \gamma_1 (1 - \delta) e^{-j\omega_e T} + a_1 g_3 + g_2 a_1/g_1. \end{aligned} \tag{20}$$

Once the coefficient γ_1 is selected, a_1, a_2, γ_2, b_1, and b_2 can be calculated based on above equations. After $Q(z) = \overline{Q}(z)$, the internal AD transfer function is simplified as

$$G_{damp}(z) = \frac{1}{z(z e^{j\omega_e T} - 1)} \times \frac{g_1 z^2 e^{2j\omega_e T} + g_2 z e^{j\omega_e T} + g_1}{z^2 e^{2j\omega_e T} - 2z e^{j\omega_e T} \cos(\overline{\omega}_{res} T) + \delta}. \tag{21}$$

Fig. 3 shows the bode diagram of $G_{damp}(z)$ of the ICF and MCF with different damping constant δ, respectively. $\overline{f}_{res}$ = 4500 Hz and $\delta = 0.8$. Regardless of the current sensor position, the proposed single-sensor AD method effectively decreases the resonance peak with arbitrary damping assignment. Additionally, the AD stability is guaranteed by the pole assignment, which

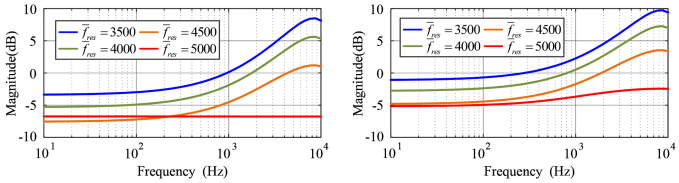

Fig. 4. Bode diagram of the $G_V(z)$ and $G_i(z)$ with different $\overline{f}_{res}$ selections and fixed $\delta = 0.8$. $f_{res} = 5400$ Hz.

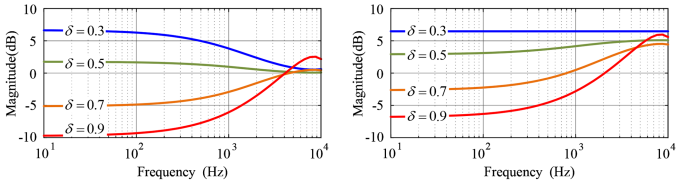

Fig. 5. Bode diagram of the $G_V(z)$ and $G_i(z)$ with different δ selections and fixed $\overline{f}_{res} = 4500$ Hz. $f_{res} = 5400$ Hz.

TABLE I
PARAMETERS OF THE EXPERIMENTAL *LCL*-EQUIPPED HSPMSM

Symbol	Parameter	Value
R	winding resistance	0.045Ω
L_1	inductance at the inverter side	54μH
L_{2o}	inductance at the machine side	27.5μH
L_s	inductance of the machine	24μH
C_1	capacitor of LCL filter	33μF
f_{res}	resonant frequency	5400Hz
U_{DC}	DC voltage	65V
$poles$	poles of the machine	2
T	control period	50μs

indicates it is effective for the *LCL* resonance within the Nyquist frequency.

B. Digital Implementation

In the digital implementation of the proposal, there are some manners that should be noted as follows:

1) V_r can be obtained by delaying the voltage reference V_r^*;
2) the coefficient μ_2 should be selected based on the current measurement as shown in (5) and (6);
3) large magnitude of $G_V(z)$ and $G_i(z)$ will deteriorate the steady-state performance when taking the system noises into account. Therefore, small magnitude of $G_V(z)$ and $G_i(z)$ is recommended; Therefore, based on the bode diagram of $G_V(z)$ and $G_i(z)$, as shown in Fig. 4, it can be found that the desired resonance frequency $\overline{f}_{res}$ should be slightly less than the real resonance frequency to achieve small $G_V(z)$ and $G_i(z)$. Without loss of generality, $\overline{f}_{res}$ can be selected as (0.8–0.9)f_{res}.
4) similar to $\overline{f}_{res}$, based on the bode diagram of $G_V(z)$ and $G_i(z)$, as shown in Fig. 5, it is recommended that the damping constant δ is located from 0.6 to 0.9.

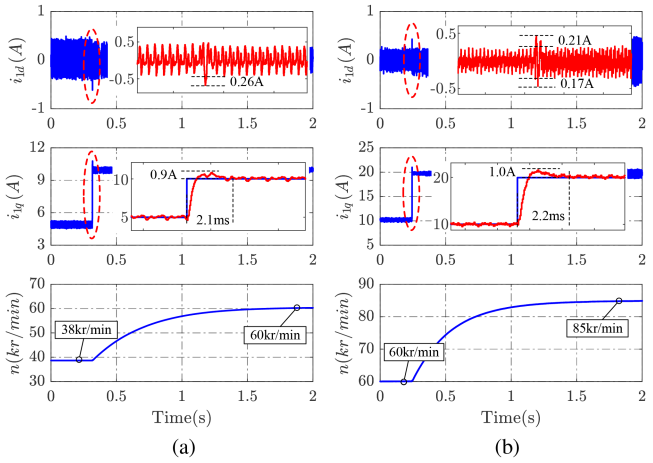

Fig. 6. Experimental results: ICF with proposed AD method when the current reference changes from 10 to 20 A.

IV. EXPERIMENTAL VALIDATIONS

Some experiments are performed to validate the proposal. The parameters of the experimental LCL-equipped HSPMSM drive system are demonstrated in Table I. A fan is connected to the shaft of the tested motor as a load, and thus the load torque is approximately proportional to the square of the motor speed. Besides, to evaluate the performance of the current controller, there is no speed control loop. Only the proposed current controller works in the experiments. $\overline{f}_{res} = 4500$ Hz, $f_{res} = 5400$ Hz, $\delta = 0.8$, $a = 0.175$, and $b = -0.174$.

Fig. 6 shows the experimental dynamic response of the proposed method with ICF. In Fig. 6(a), at $t = 0.3$ s, i_{1q}^* has s stepping change from 5 to 10 A. With the proposed method, i_{1q} effectively tracks the reference with a rise time of about 2.1 ms and an overshoot of about 0.9 A. Meanwhile, the tested motor accelerates from 38 k/min(633 Hz) to 60 kr/min(1000 Hz). In Fig. 6(b), the current reference i_{1q}^* changes from 10 to 20 A and the current i_{1q} reaches the steady state with a rise time of about 2.2 ms and an overshoot of about 1.0 A. Meanwhile, the speed is accelerated to 85 k/min(1417 Hz). Fig. 7 shows the experimental dynamic response of the proposed method with MCF. In Fig. 7(a), at $t = 0.2$ s, the i_{2q}^* varies from 5 A to 10 A. By proposal, i_{2q} effectively tracks the reference with a rise time of about 2.7 ms and an overshoot of about 0.4 A. In Fig. 7(b), the current reference i_{2q}^* changes from 10 to 20 A and thus the speed is up to 82 k/min(1367 Hz). By the proposed method, i_{2q} achieves the reference tracking with a rise time of about 1.2 ms and an overshoot of about 0.25 A.

The robustness against the variation of the motor inductance is also validated by experiments with ICF and MCF, as shown in Fig. 8 and Fig. 9, respectively. It can be easily observed that both the stability and the dynamic performance of the proposal are well ensured when the motor inductance varies $\pm 50\%$ of the real value.

Additionally, to validate theoretical analysis of the proposed AD method, the critical damping constant δ is experimentally tested. Based on the ideal damped transfer function in (21), when

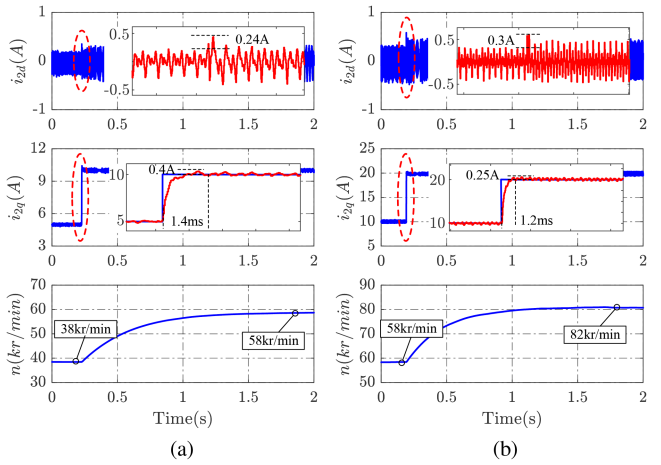

Fig. 7. Experimental results: MCF with proposed AD method. From top to down: i_{2d}, i_{2q}, and speed (kr/min).

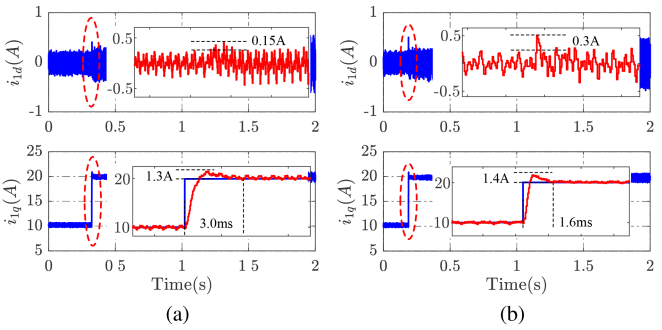

Fig. 8. Experimental results: ICF with the mismatched motor inductance.

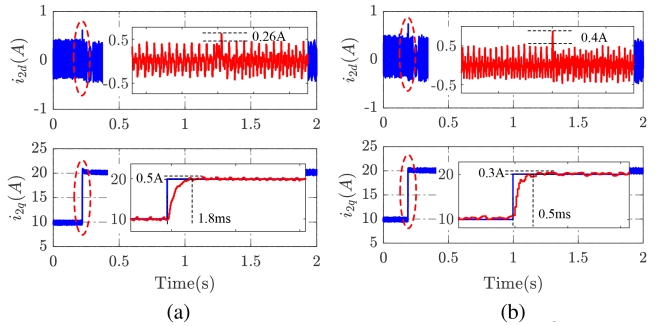

Fig. 9. Experimental results: MCF with the mismatched motor inductance.

δ is selected as 1, the open-loop drive system has a new resonance pole pair, where the frequency is $\overline{\omega}_{res} \pm \omega_e$. Considering the current controller (9) has negligible effects on the resonance poles, $\delta = 1$ can be regarded as the theoretical critical damping constant. When $\delta < 1$, the closed-loop system is stable. $\delta > 1$ means unstable. Fig. 10 shows the experimental results of the critical damping constant δ with ICF and MCF. The initial δ is 0.8 and it will increase as a ramp to 1.1. For ICF, as shown in Fig. 10(a), after δ reaches about 1.04, the fluctuation of the current i_{1q} has gradually enlarged as the continuously increasing

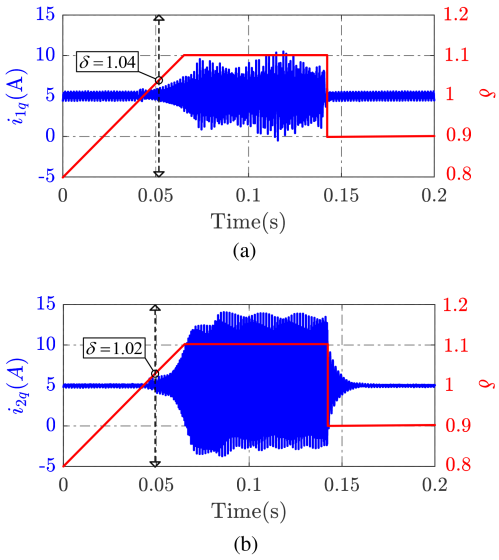

Fig. 10. Experimental results: the critical damping constant δ testing.

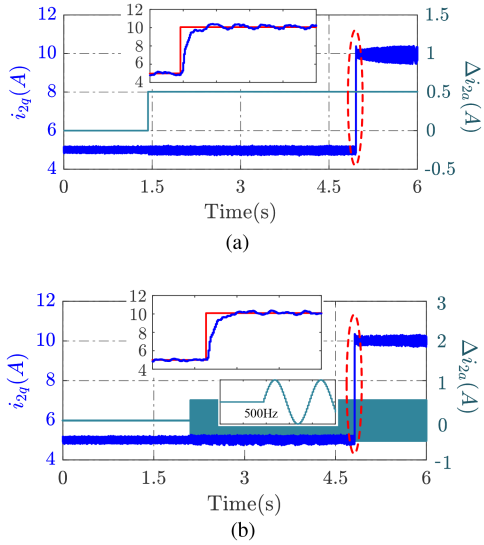

Fig. 11. Experimental results: current control performance with stepping offset disturbance and sinusoidal wave disturbance in i_{2a}.

δ. It can be concluded that the critical damping constant δ is around 1.04 in the tested drive system. Once δ returns to 0.9, the fluctuation of i_{1q} is greatly reduced, which indicates the AD works again. For MCF, as shown in Fig. 10(b), the tested critical δ is about 1.02. Based on the experimental results, the tested critical δ is much close to the theoretical value. Therefore, the feasibility of the theoretical analysis in this article is validated.

Fig. 11 shows the experimental results of the proposed current control performance when the stepping offset disturbance and sinusoidal wave disturbance occur in the measurement of i_{2a}. Without loss of generality, the stepping offset disturbance is selected as $\Delta i_{2a} = 0.5$ A and the sinusoidal wave disturbance is $\Delta i_{2a} = 0.5 \sin(1000\,\pi t)$A. It can be observed that the proposal has good robustness against the current measurement error resulting from the sampling disturbance.

V. Conclusion

This letter proposed a general single-sensor AD framework for *LCL*-equipped HSPMSMs in the synchronous coordinate, which was suitable for ICF and MCF drive systems. The simplified analytical expression between the physical parameters and the damping performance was provided, which enables automatic tuning for different drive systems. By the proposal, arbitrary damping assignment and stability for the *LCL* resonance within the Nyquist frequency were achieved. Finally, the experimental results validate the effectiveness and robustness of the developed AD controller.

References

[1] D. Gerada, A. Mebarki, N. L. Brown, C. Gerada, A. Cavagnino, and A. Boglietti, "High-speed electrical machines: Technologies, trends, and developments," *IEEE Trans. Ind. Electron.*, vol. 61, no. 6, pp. 2946–2959, Jun. 2014.

[2] W. Yao, Y. Yang, X. Zhang, F. Blaabjerg, and P. C. Loh, "Design and analysis of robust active damping for LCL filters using digital notch filters," *IEEE Trans. Power Electron.*, vol. 32, no. 3, pp. 2360–2375, Mar. 2017.

[3] S. G. Parker, B. P. McGrath, and D. G. Holmes, "Regions of active damping control for LCL filters," *IEEE Trans. Ind. Appl.*, vol. 50, no. 1, pp. 424–432, Jan./Feb. 2014.

[4] X. Wang, F. Blaabjerg, and P. C. Loh, "Virtual RC damping of LCL-Filtered voltage source converters with extended selective harmonic compensation," *IEEE Trans. Power Electron.*, vol. 30, no. 9, pp. 4726–4737, Sep. 2015.

[5] E. Rodriguez-Diaz, F. D. Freijedo, J. C. Vasquez, and J. M. Guerrero, "Analysis and comparison of notch filter and capacitor voltage feedforward active damping techniques for LCL grid-connected converters," *IEEE Trans. Power Electron.*, vol. 34, no. 4, pp. 3958–3972, Apr. 2019.

[6] X. Wang, F. Blaabjerg, and P. C. Loh, "Grid-current-Feedback active damping for LCL resonance in grid-connected voltage-source converters," *IEEE Trans. Power Electron.*, vol. 31, no. 1, pp. 213–223, Jan. 2016.

[7] L. Zhou et al., "Inverter-current-Feedback resonance-suppression method for LCL-Type DG system to reduce resonance-frequency offset and grid-inductance effect," *IEEE Trans. Ind. Electron.*, vol. 65, no. 9, pp. 7036–7048, Sep. 2018.

[8] E. Wu and P. W. Lehn, "Digital current control of a voltage source converter with active damping of LCL resonance," *IEEE Trans. Power Electron.*, vol. 21, no. 5, pp. 1364–1373, Sep. 2006.

[9] R. A. Fantino, C. A. Busada, and J. A. Solsona, "Observer-based grid-voltage sensorless synchronization and control of a VSI-LCL tied to an unbalanced grid," *IEEE Trans. Ind. Electron.*, vol. 66, no. 7, pp. 4972–4981, Jul. 2019.

[10] M. A. Awal, L. D. Flora, and I. Husain, "Observer based generalized active damping for voltage source converters with LCL filters," *IEEE Trans. Power Electron.*, vol. 37, no. 1, pp. 125–136, Jan. 2022.

[11] J. Kukkola, M. Hinkkanen, and K. Zenger, "Observer-based state-space current controller for a grid converter equipped with an LCL filter: Analytical method for direct discrete-time design," *IEEE Trans. Ind. Appl.*, vol. 51, no. 5, pp. 4079–4090, Sep./Oct. 2015.

[12] C. A. Busada, S. G. Jorge, and J. A. Solsona, "Full-state feedback equivalent controller for active damping in LCL-Filtered grid-connected inverters using a reduced number of sensors," *IEEE Trans. Ind. Electron.*, vol. 62, no. 10, pp. 5993–6002, Oct. 2015.

[13] J. Wang, J. D. Yan, L. Jiang, and J. Zou, "Delay-dependent stability of single-loop controlled grid-connected inverters with LCL filters," *IEEE Trans. Power Electron.*, vol. 31, no. 1, pp. 743–757, Jan. 2016.

[14] Y. Yao, Y. Huang, F. Peng, J. Dong, and Z. Zhu, "Dynamic-decoupled active damping control method for improving current transient behavior of LCL-Equipped high-speed PMSMs," *IEEE Trans. Power Electron.*, vol. 37, no. 3, pp. 3259–3271, Mar. 2022.